Induced polarization of volcanic rocks. Part 7. Kimberlites

K Titov, V Abramov, V Emelianov, André Revil

Geophysical Journal International

Geophys. J. Int. (2024) **236,** 233–248
Advance Access publication 2023 October 16
GJI Geomagnetism and Electromagnetism

https://doi.org/10.1093/gji/ggad396

Induced polarization of volcanic rocks. Part 7. Kimberlites

K. Titov [1], V. Abramov,[1,2] V. Emelianov [1] and A. Revil [3]

[1] *Institute of Earth Sciences, St. Petersburg State University,* 7-9 *Universitetskaya naberezhnaya,* 199034, *St. Petersburg, Russia. E-mail: k.titov@spbu.ru*
[2] *Vilyuyskaya Geological Exploration Expedition, PJSC ≪ALROSA≫,* 7*B, ul. Vilyuyskaya, Mirny,* 678174, *Republic of Sakha (Yakutia), Russia*
[3] *Université Grenoble Alpes, Univ. Savoie Mont-Blanc, CNRS, UMR CNRS* 5204, *EDYTEM,* 73370 *Le Bourget du Lac, France*

Accepted 2023 September 30. Received 2023 September 29; in original form 2023 July 29

SUMMARY

In the field, kimberlites are characterized by high electrical conductivities (about 0.1 S m^{-1}) compared to most igneous rocks. The reason for these high conductivities has not been fully elucidated to date. We investigate here the spectral induced polarization of seven core samples of kimberlites in the frequency range 1.43 mHz–20 kHz. The measurements are made at pore water conductivities ranging from 0.07 to 2.4 S m^{-1} (NaCl, 25 °C). We also measured the cation exchange capacity (CEC), the specific surface area (SSA) and the magnetic susceptibility of the core samples. We characterized the samples by optical microscopy as well as the X-ray diffraction and thermogravimetric analyses. Based on the electrical measurements, we obtained values of the surface conductivity produced by the double electrical layer coating the solid particles, and the normalized chargeability values characterizing the polarization magnitude of these materials. Mineralogical analyses show significant amount of magnetite (from 2 to 9 wt. per cent, approximately 1 to 4 per cent in vol. content) and smectite (from 1 to 44 wt. per cent) in the core samples. The main contributor of the CEC is smectite because of its very high CEC. The quadrature conductivity, the normalized chargeability, and the surface conductivity are controlled by the CEC normalized by the tortuosity of the pore space (product of the formation factor by the porosity). Our data demonstrate that the conduction and polarization of kimberlites are both controlled by the presence of smectite rather than associated with magnetite. Comparing the new data set and data recently obtained with volcanic rocks from both shield and strato-volcanoes in the previous papers of this series, we show that the model of polarization of the dynamic Stern layer correctly describes the complex electrical conductivity of kimberlites as well. Our results also explain the cause of electrical conductivity anomalies detected at kimberlite pipes and offer new perspectives in using induced polarization method for the exploration of kimberlites around the world.

Key words: Electrical properties; Electromagnetic theory; Induced polarization; Kimberlite; Volcanoes.

1 INTRODUCTION

Kimberlite presents an important source of diamonds around the world (e.g. Hawthorne 1975; Field & Scott Smith 1999; Coopersmith *et al.* 2006). Being igneous ultramafic rocks, kimberlites originate from the Earth mantle from depths of at least 150–450 km (Kjarsgaard 2007). The kimberlite magma transports to the Earth surface xenoliths of the mantle material may include diamonds (e.g. Smit & Shirey 2019 for a clear and concise review). For these reasons, kimberlites have attracted a lot of attention over the past century.

Unaltered kimberlite is of porphyritic texture with inclusions of olivine, pyrope (a dark, blood-red gemstone), chromian diopside (a pyroxene mineral), magnesian ilmenite (a titanium-iron oxide mineral) and phlogopite (a magnesium mica belonging to the family of phyllosilicates) surrounded by a finer-grained matrix (Mitchell 1986, 1995). The matrix consists of microphenocrysts of olivine, Mg–Cr–Ti-rich spinel, monticellite, mica (phlogopite–kinoshitalite solid solutions), perovskite, apatite and occasionally calcite, all set in a late-stage groundmass of carbonates (calcite and/or dolomite) and serpentine produced by the alteration of olivine (Afanasyev *et al.* 2014; Mitchell *et al.* 2019). Depending on the alteration degree, the groundmass contain smectites produced by the alteration of serpentine (e.g. Ji *et al.* 2018). In addition, magnetite is produced from the alteration of olivine (e.g. Kononova *et al.* 2007). Kimberlite breccia also include fragments of the surrounding rocks, whereas autolithic kimberlites include kimberlite material of previous phases of eruption (e.g. Kononova *et al.* 2007, for examples of kimberlites from the Archangelsk Region in Russia). If not all kimberlites contain smectites (see Morkel & Vermaak 2006), Morkel

et al. (2007) state '*Kimberlite commonly contains smectite minerals (such as montmorillonite and saponite), which cause fragmentation or degradation of the rock when it is exposed to water or aqueous solutions*'.

An experience obtained during about 50 yr of field geophysical surveys around the world shows very different values of the kimberlite electrical conductivity ranging from about 10^{-4} S m^{-1} (Katsube & Kjarsgaard 1994 for Canada, North-West territories) to more than 0.1 S m^{-1} (Onugba *et al.* 1989 for Northern Nigeria). Obviously, in Arctic Regions, the presence of permafrost may play a strong role on the effective conductivity. Nevertheless, most of kimberlites are characterized by high electrical conductivity comparing to other igneous or metamorphic rocks (e.g. Macnae 1979; Power *et al.* 2004; Reed & Witherly 2007). Crater facies kimberlite often contains significant clays other than the kimberlite source, and is conductive even if smectite is not present in the underlying hypabyssal phase of the kimberlite (Macnae 1979). The goal of our study is to investigate the cause of such high electrical conductivity of kimberlites following preliminary works by Macnae (1979), Titov *et al.* (2021) and Emelyanov *et al*. (2020).

In this paper, we present new data concerning the complex electrical conductivity, mineralogical composition and physical–chemical properties of seven samples taken in kimberlite pipes located in northeastern Angola (Africa). Beside complex conductivity measurements, we also determine the cation exchange capacity (CEC), the specific surface area (SSA), the mineralogical composition and the magnetic susceptibility (MS) of our core samples. The scientific question we tackle in this work is to know what mineral phase controls the complex conductivity of kimberlites. We also compare new results with those obtained in previous papers of this series (Revil *et al.* 2017a, 2021; Zhang *et al.* 2023). We are especially interested to compare the electrical behaviour of kimberlites and basalts at various levels of alteration.

The paper is organized as follow. We first briefly describe the geological setting of the kimberlite deposit of Cuilo in Angola, where we sampled the cores used below. Then, in Section 3, we present the core samples and the methodologies used to acquire the petrophysical properties of interest. Then, we discuss the results in terms of relationship between the parameters and the underlying physical mechanisms at play to understand the complex conductivity of kimberlites.

2 MATERIAL AND METHODS

2.1. Materials

The Cuilo kimberlite field (Fig. 1) of Cretaceous age is located in the northeastern Angola within the Kasai craton. In this area, the Lucapa fault zone has a major role in the distribution of kimberlite fields including the famous Catoca field known by very rich in diamonds (Pettit 2009; Cruz 2012). The Kasai craton is an area of high diamond production in Central Africa (Zagainy *et al.* 2017). The kimberlite pipes of the Cuilo field were discovered by an airborne magnetic survey (1:10 000 scale, Eley *et al.* 2008). Indeed, they exhibit pronounced magnetic anomalies because the MS of the host rocks is sufficiently smaller than the MS of the kimberlites.

In the Kasai craton, host rocks include Archean granite and gneiss basement. We also find Triassic-Jurassic sediments of the Karoo supergroup including siltstones, shales and sandstones. The kimberlite bodies are covered by the Cretaceous Calonda unconsolidated sands, the Palaeogene-Neogene Kalahari sands and Quaternary deposits also composed mostly by sands. The total thickness of the sedimentary cover is about 50 ms. Small levels of kimberlite erosion in the area have led to a preservation of crater facies. The crater deposits are mostly composed of kimberlite breccia and tuff sandstone with kimberlite materials while the diatremes present porphyritic and autolithic kimberlites (Eley *et al.* 2008; Pettit 2009).

We studied seven cores sampled at different levels of the kimberlite pipes (Fig. 2). The cores samples include two porphyritic kimberlites (labelled AC-01–01/182 and AC-01–01/201), three autolithic kimberlites (labelled AC-05–05/209, AC-254–01/104 and AC-23–01/70), a fine-grained kimberlite breccia (labelled AC-16–14/45) and a tuff sandstone with gravels mixed with kimberlite materials (labelled Alt-60–08/364). At the initial (reference) state, all the core samples are consolidated kimberlites. The cores are cylinders with a diameter of 4.7 cm and a length between 3.0 and 4.9 cm. They were received partially water-saturated and the salinity of the initial pore water was unknown. Because of the swelling pressure associated with the presence of smectite, these cores are very fragile and difficult to measure. The risk is the disaggregation of the core samples when solutions are used that are too far from their equilibrium state.

2.2 Core sample characterization

We characterized the kimberlite core samples using optical microscopy, X-ray diffraction analysis (XRD), thermogravimetric analysis (TGA), and the measurements of their CEC, SSA, MS and complex electrical conductivity spectra at 5–8 pore water salinities (NaCl, 25 °C).

The XRD analysis provides information about the mineralogical composition of the core samples. We performed XRD using the DRON-8 diffractometer with vertical theta–theta goniometer and sample horizontal position (see https://www.bourevestnik.ru/products/analiticheskaya-tekhnika/rentgenodifraktsionnyy-analiz/mnogofunktsionalnyy-rentgenovskiy-difraktometr-dron-8-8n/).

The TGA is based on measurements the mass of a sample over time as the temperature increases. These measurements provide information about phase transitions and chemical decompositions of minerals allowing determination a mineral composition (e.g. Coats & Redfern 1963). We used the DTG60H synchronous thermal analyser (see https://www.shimadzu.com/an/products/thermal-analysis/simultaneous-thermal-analysis/dtg-60-series/index.html).

We also measured the CEC to characterize the amount of exchangeable cations on the minerals surface. The CEC is often used as a proxy of the electrical double-layer properties, especially for alumino-silicates such as smectite. Smectite is known to have the largest CEC of all minerals (∼80–100 meq/100 g). We used the standard method by Food and Agriculture Organization of the United Nations (Standard 2022). The method is based on absorption of the magnesium acetate, which has a high affinity for the mineral surface.

We determined the SSA using the Brunauer–Emmett–Teller method based on the nitrogen adsorption (Brunauer *et al.* 1938). We carried out the measurements using an ASAP 2020 MP specific surface analyser (https://www.micromeritics.com/asap-2020-plus/). We measured CEC and SSA with small subsamples of the main core samples used for the complex conductivity measurements.

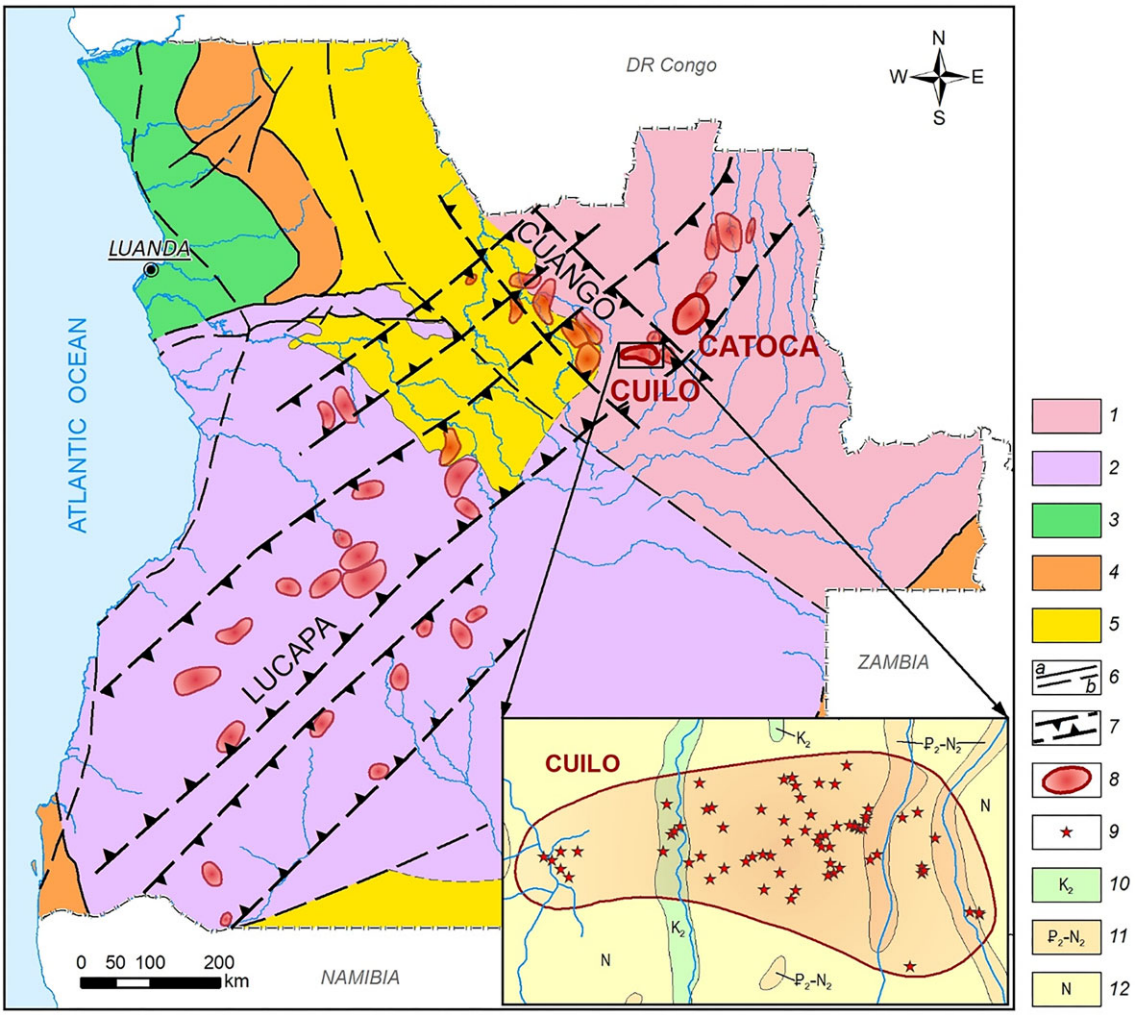

Figure 1. Cuilo kimberlite field (Angola). Archean cratons: 1—Kasai and 2—Angolan. Mobile belts: 3—Palaeoproterozoic (Eburnean) and 4—Neoproterozoic (Pan-African). 5—Riftogenic Meso-Neoproterozoic sedimentary basins. 6—faults apparently not related to the kimberlite magmatism (a—major and b—subordinate). 7—faults of Nord-West and Nord-East strike related to kimberlite eruptions. 8—kimberlite fields. 9—kimberlite pipes. Ages: 10—upper Cretaceous, 11—Eocene-Pliocene (Kalahari group) and 12—Neogene (Kalahari group, Ocre sand formation).

We measured the MS with the SM-30 kappa-meter (ZH instruments, http://www.zhinstruments.com/sm_30.html). For each sample, we performed at least 10 measurements on each side, followed by an arithmetic averaging of the data set for each core sample. We also determined the sample porosity and mass density with the standard triple weighting method.

2.3 Sample saturation methodology

Because we measured the complex electrical conductivity at different values of the pore water conductivities, we have paid special attention to saturation of the samples with brines. These so-called multisalinity experiments allow accurate determination of the formation factor F and the surface conductivity σ_S of samples (e.g. Waxman & Smits 1968). We decided to start with the highest salinity. Indeed, some core samples are very rich in smectite (see Table 1), and saturation with low salinity pore waters could produce an increased swelling pressure leading to the collapse of the samples structure and integrity. In addition, because the initial pore brine salinity is unknown, it was reasonable to start with the highest salinity brine to be sure that we can neglect the residual salt being in the pore space after the heating of the sample as discussed below.

We started with the sample heated in an oven at 70 °C up until their weights reached a plateau. Then, we saturated the samples under vacuum with degassed water (NaCl, 2.4 S m^{-1}, at 24 °C). Based on the triple weighting procedure (dry, saturated and buoyancy weight in distilled water), we obtained values of both the bulk density and connected porosity (Table 2). Then, we controlled the procedure of the sample equilibration with water by monitoring the sample complex electrical conductivity. The equilibration takes about 1–2 months for each change of salinity. After a first series of the complex conductivity measurements (see Section 3.2.4 below), we put each core sample in an individual container with the less salty water and we waited about 1–2 months for the next equilibrium to be reached between the sample and the new pore water. We kept the pre-determined value of the water conductivity in the container, and we monitored the sample complex electrical conductivity several times up to stabilization of the complex conductivity values. We followed this sequence of the sample 'desalting' procedure several times. Finally, we obtained the complex conductivity data at the water conductivity values of 2.40, 1.86, 1.57, 1.22, 0.79, 0.45, 0.26,

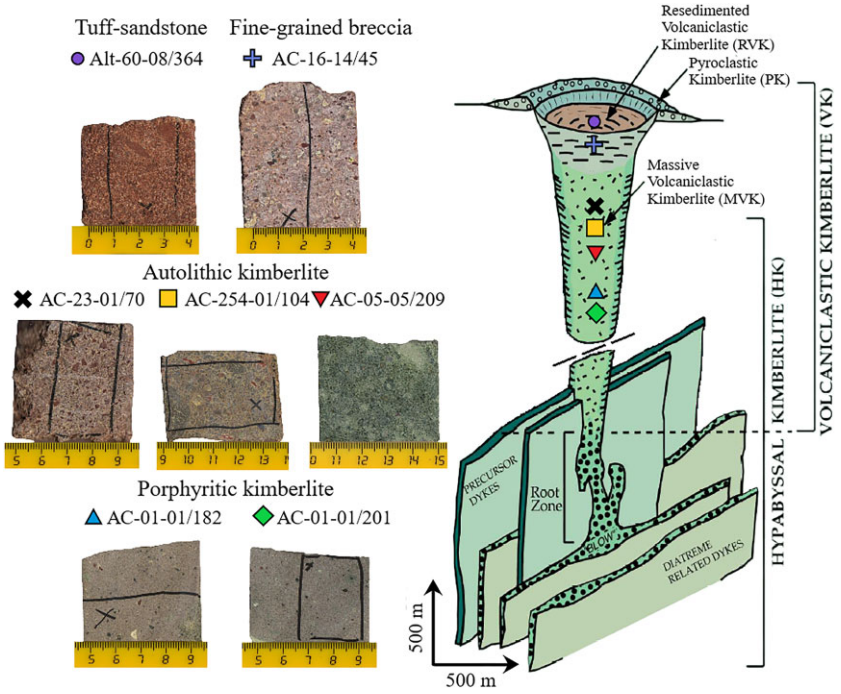

Figure 2. Location of the cores along with the conceptual model of the kimberlite pipe (modified from Kjarsgaard 2007) called the 'classic South African model' of a kimberlite pipe (see Mitchell 1986, 1995; Kjarsgaard 2003; Sparks *et al.* 2006). The scales are very approximate.

0.11 and 0.07 S m^{-1} (25 °C). We completed the measurements in one year and a half.

2.4 Induced polarization

The electrical conductivity of porous media (rocks, soils, sediments, suspensions, biological tissues, etc.) is the complex-valued quantity. Its real part is a measure of the conduction, whereas the imaginary part characterizes the polarization (e.g. Olhoeft 1981; Kralchevsky *et al.* 2008). In the low-frequency range (up to about several tens of kilohertz), the overall polarization is dominated by the Eectrical Double Layer (EDL) polarization or/and a specific polarization of semiconducting or electronically conducting minerals like, for example, graphite, magnetite and pyrite (Wong 1979; Olhoeft 1981; Revil *et al.* 2015a). In geophysics, this low-frequency polarization is called 'induced polarization' (e.g. Olhoeft 1981; Revil 2013a).

The low-frequency polarization denotes a set of mechanisms with the reversible accumulation and depletion of the electrical charge carriers in porous media. The phenomena are characterized by characteristic (relaxation) times depending on the characteristic length of the elements undergoing polarization (grain or pore sizes). Measurement of the complex resistivity or its inverse, the complex conductivity, in the frequency range from several millihertz to several kilohertz is known as the spectral induced polarization (SIP) method allowing characterization of a distribution of such characteristic (or relaxation) times (e.g. Nordsiek & Weller 2008).

The complex-valued electrical conductivity, σ^* (or its inverse, the complex electrical resistivity, ρ^*),

$$\sigma^*(\omega) = \sigma'(\omega) + i\sigma''(\omega) = |\sigma^*(\omega)|\, e^{i\varphi(\omega)}, \tag{1}$$

$$\rho^*(\omega) = \frac{1}{\sigma^*(\omega)}, \tag{2}$$

are obtained based on field or laboratory experiments. Here, $\omega = 2\pi f$ is the angular frequency of the field (in rad s^{-1}), f is the frequency (in Hz), $\sigma'(\omega)$ and $\sigma''(\omega)$ are the real and imaginary components of the resistivity, respectively (in Ω·m), i is the (pure) imaginary unit defined as $i^2 = -1$ and $\varphi(\omega)$ is the phase shift (in rad) between the voltage and current signals.

In laboratory, the complex impedance, $Z^*(f)$, is typically measured. The complex resistivity is proportional to the impedance,

$$\rho^* = kZ^*, \tag{3}$$

where k (in m) is the geometrical factor obtained by measurements with water samples of known electrical conductivity or by numerical calculations on the basis of known sample and measurement setup geometry (e.g. Jougnot *et al.* 2010). Because the sample lengths were different, we used holders of different length and we obtained the geometrical factor values for each holder based on the conductance measurements with the water samples of known electrical conductivity.

Although we measured the amplitude and phase of the impedance, in interpretation we mostly use the complex electrical conductivity. We obtained the conductivity based on eq. (2) and the elementary complex algebra:

$$\sigma' = |\sigma^*| \cos\varphi, \tag{4}$$

$$\sigma'' = |\sigma^*| \sin\varphi. \tag{5}$$

By convention, we consider here and below the negative conductivity phase, and, therefore, the negative quadrature conductivity.

For ion-conducting rocks, soils and sediments we assume two kinds of conduction acting in parallel: the volume conduction acting along the free pore water, and the surface conduction along EDL. For more complex model, refer to, for example, Kan & Sen (1987), Revil *et al.* (2015a) and Misra *et al.* (2016a,b), who discussed the conductivity model without the assumption about the parallel connection. The surface conduction acts along the interface between the solid and liquid phases in EDL because of some excess of ions

Table 1. Mineralogical composition of kimberlite according to XRD and TGA.

Sample	Description	Components (wt. per cent)												
		Serpentine	Smectite	Quartz	Calcite	Chlorite	Mica	Siderite	Haematite and magnetite	Perovskite	Diopside	Kaolin	Hydromica	Unidentified amorphous phases, non-thermoactive phases: iron silicon oxides, etc.
AC-05 -05/209	Autolithic kimberlite	76	11	1	6	–	6	–	–	–	–	–	–	–
AC-254–01/104		72	12	1	12	–	–	3	–	–	–	–	–	–
AC-23–01/70		–	44	–	20	–	–	–	2	–	–	–	–	34
AC-01–01/182	Porphyritic kimberlite	39	5	–	12	12	9	3	9	11	–	–	–	–
AC-01–01/201		28	1	7	16	–	27	4	8	4	3	–	–	2
AC-16–14/45	Fine-grained kimberlite breccia	–	32	34	15	–	–	–	2	–	–	–	5	12
Alt-60–08/364	Tuff sandstone	–	20	67	4	–	3	–	–	–	–	5	–	1

Table 2. Physical–chemical properties of the kimberlite samples. ϕ, F and m are the dimensionless porosity, formation factor and cementation exponent, respectively; σ'_s (in mS m^{-1}) is the real part of the surface conductivity (at 1.46 Hz); σ'' (in mS m^{-1}) is the imaginary part of the complex conductivity (at 1.46 Hz and $\sigma_w \sim 0.8$ S m^{-1}) and M_n (in m m^{-1}) is the normalized chargeability (at $\sigma_w \sim 0.8$ S m^{-1}). The units of CEC, SSA and MS are meq/100 g, m^2 g^{-1}, and 10^{-5} in the international unit system, respectively.

Sample	Description	ϕ	F	m	σ'_s	σ''	M_n	CEC	SSA	MS
AC-05–05/209	Autolithic kimberlite	0.23	32.3	1.85	54	0.522	5.19	15.41	40.3	107
AC-254–01/104		0.25	18.5	2.01	140	1.13	10.6	18.53	17.7	1202
AC-23–01/70		0.18	15.4	2.04	260	3.98	36.5	66.22	41.7	2328
AC-01–01/182	Porphyritic kimberlite	0.22	52.9	2.63	7.7	0.204	1.88	7.41	11.7	11 365
AC-01–01/201		0.13	66.7	2.04	11	0.105	1.60	6.73	12.9	12 074
AC-16–14/45	Fine-grained kimberlite breccia breccia	0.23	10.0	1.57	65	2.45	19.3	23.05	20.76	180
Alt-60–08/364	Tuff sandstone with kimberlite material	0.19	12.7	1.52	145	3.19	21.9	32.6	25.5	31

near the solid surface comparing to the free water far from the pore walls (e.g. Revil & Glower 1998).

Electrical double layer contains two sublayers: the Stern layer and the diffuse layer. The Stern layer of weakly sorbed counterions directly coats the solid surface, the ions have a tangential mobility only. In the diffuse layer (between the Stern layer and the free pore water) the counter- and co-ions can move in both the tangential and normal direction relative to the interface (e.g. Leroy *et al.* 2008, and references therein). In addition, the ion diffusivity in the free water, the diffuse layer, and the Stern layer of quartz is assumed to have the same value of about 1.3×10^{-9} m^2 s^{-1} (for Na^+ at 25 °C). In contrast, for the Stern layer at alumino-silicates (clay) surface, the diffusivity value was assessed to be as low as 3.8×10^{-12} m^2 s^{-1} (e.g. Revil *et al.* 2015b).

Accounting both kinds of conduction, the expression of the real (in-phase) conductivity in fully water-saturated conditions is

$$\sigma'(\omega) = \frac{\sigma_w}{F} + \sigma'_s(\omega). \tag{6}$$

Here, σ_w denotes the pore water conductivity (in S m^{-1}), ϕ and F denote the dimensionless porosity and formation factor and $\sigma'_s(\omega)$ is the real part of the surface conductivity in S m^{-1} (e.g. Revil 2013a). According to the first Archie's (1942) law,

$$F = \phi^{-m}, \tag{7}$$

where m (dimensionless) is called the first Archie exponent, which characterizes the pore space topology/texture. Consequently, the pore space tortuosity is $\theta = \phi F$.

In absence of electronically conducting or semiconducting minerals, we consider the EDL polarization only, therefore the quadrature (imaginary) conductivity depends only on the properties of the surface of the grains:

$$\sigma''(\omega) = \sigma''_s(\omega). \tag{8}$$

An individual value of the quadrature conductivity at a certain frequency represents a local polarization effect related to a specific frequency. In contrast, the global polarization effect is characterized by the total normalized chargeability,

$$M_n = \sigma_\infty - \sigma_0, \tag{9}$$

where σ_∞ and σ_0 (in S m^{-1}) are the high (or instantaneous) and low (DC, direct current) frequency limits of the electrical conductivity, respectively. The normalized chargeability can be obtained by different ways. A popular approach is to approximate experimental data using phenomenological models like the Cole–Cole model (Cole and Cole 1941) or the Pelton model (Pelton *et al.* 1978). By the best fit to data, four parameters: the chargeability, the main time constant, the DC resistivity and the Cole–Cole exponent can be obtained.

An alternative approach is a so-called Debye decomposition (e.g. Nordsiek & Weller 2008). With this approach, the complex resistivity or conductivity is represented as a superposition of Debye relaxation models (Debye 1929). In the discrete form, the governing equation of the Debye decomposition method for the complex resistivity is

$$\rho^*(\omega) = \rho_0 \cdot \left(1 + \sum_{k=1}^{N_\tau} m_k \cdot \left(1 - \frac{1}{1 - i\omega\tau_k}\right)\right), \tag{10}$$

where ρ_0 is the DC resistivity (in Ohm), $m_k(\tau_k)$ are the dimensionless magnitudes of polarization (the partial chargeabilities) at certain characteristic times, τ_k (in s) and N_τ is the number of the characteristic times. Then, the normalized chargeability (in S m^{-1}) is

$$M_n = \sum_{k=1}^{N_\tau} m_k \sigma_\infty, \tag{11}$$

where the instantaneous conductivity is given by

$$\sigma_\infty = \frac{1}{\rho_0 \left(1 - \sum_{k=1}^{N_\tau} m_k\right)}. \tag{12}$$

In this paper, we used the Debye decomposition to calculate the normalized chargeability. That said, we could also use the Cole–Cole model approach developed by Revil (2013a, b) as an alternative approach to model both the induced polarization response and the Maxwell–Wagner polarization response of the material.

We consider a granular model of kimberlite where clay tactoids of the groundmass and inclusions within the matrix are surrounded by the pore water. The Stern and diffuse layers formed the so-called electrical double layer coating the surface of the grains. We consider polarization of the Stern layer, assuming polarization of the diffuse layer is second-order effect. The aforementioned statements represent the basis of the polarization model of the dynamic Stern layer (e.g. Leroy *et al.* 2008; Revil 2013a,b, and references therein). This model leads to the following proportionality relationships between the electrical parameters (see also Weller *et al.* 2013; Revil *et al.* 2015b):

$$M_n = a\frac{\mathrm{CEC}}{F\phi}, \tag{13}$$

$$M_n = R\sigma_s, \tag{14}$$

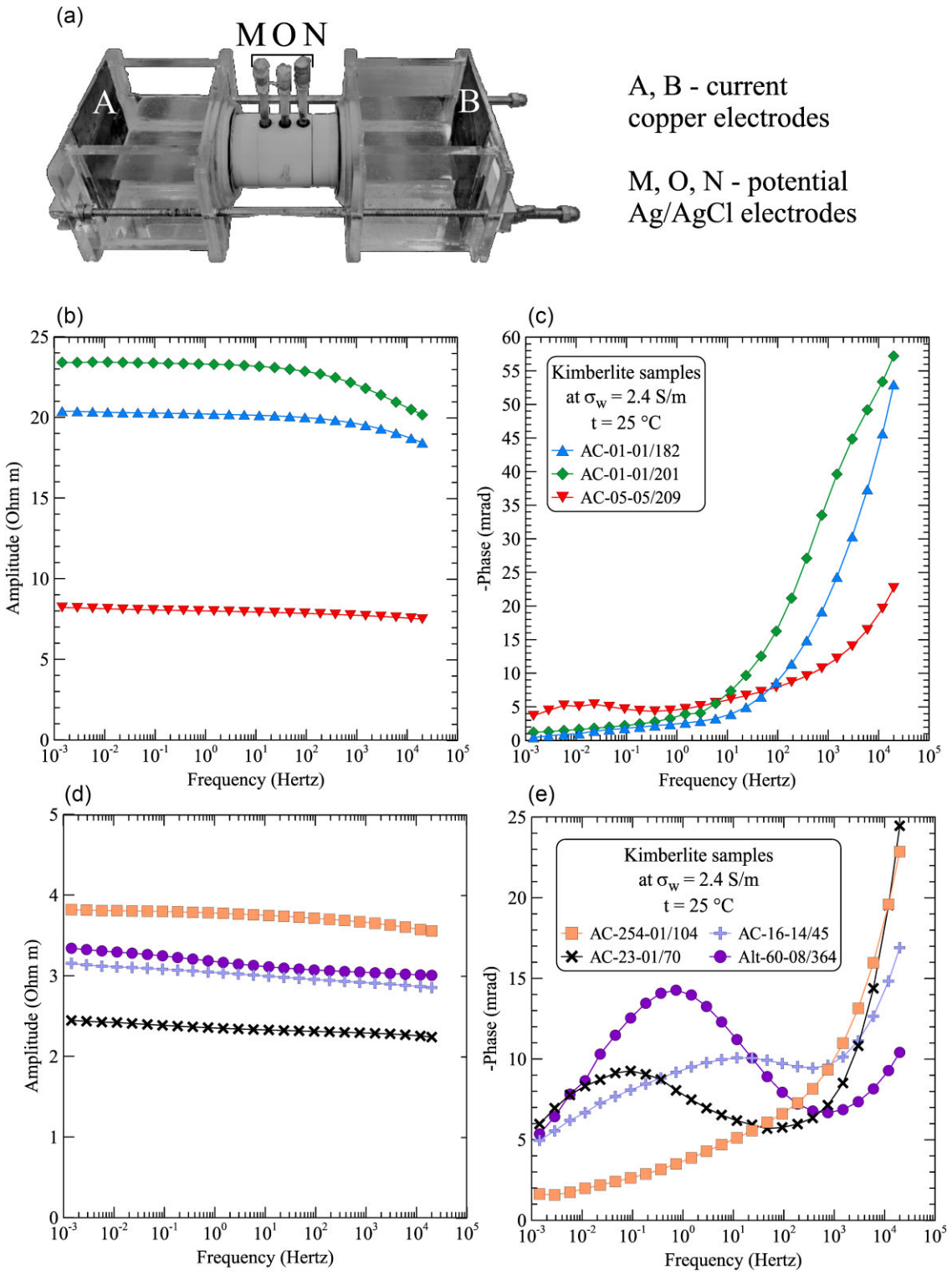

Figure 3. (a) Sample holder and (b) illustration of the data reproducibility. (a) The jacketed sample is squeezed between the two small tanks. A and B are the copper current plate electrodes for the injection/retrieval of the electrical current, and M, O, N are the Ag/AgCl potential electrodes. (b) and (d) are the real part of the resistivity, and (c) and (e) are the phase of the resistivity. The measurement uncertainty is significantly less than the symbols size. Symbols identify the samples: AC-01–01/182 and AC-01–01/201 are the porphyritic kimberlites; AC-05–05/209, AC-254–01/104 and AC-23–01/70 are the autolithic kimberlite; AC-16–14/45 is the fine-grained breccia and Alt-60–08/364 is the tuff sandstone with kimberlite material.

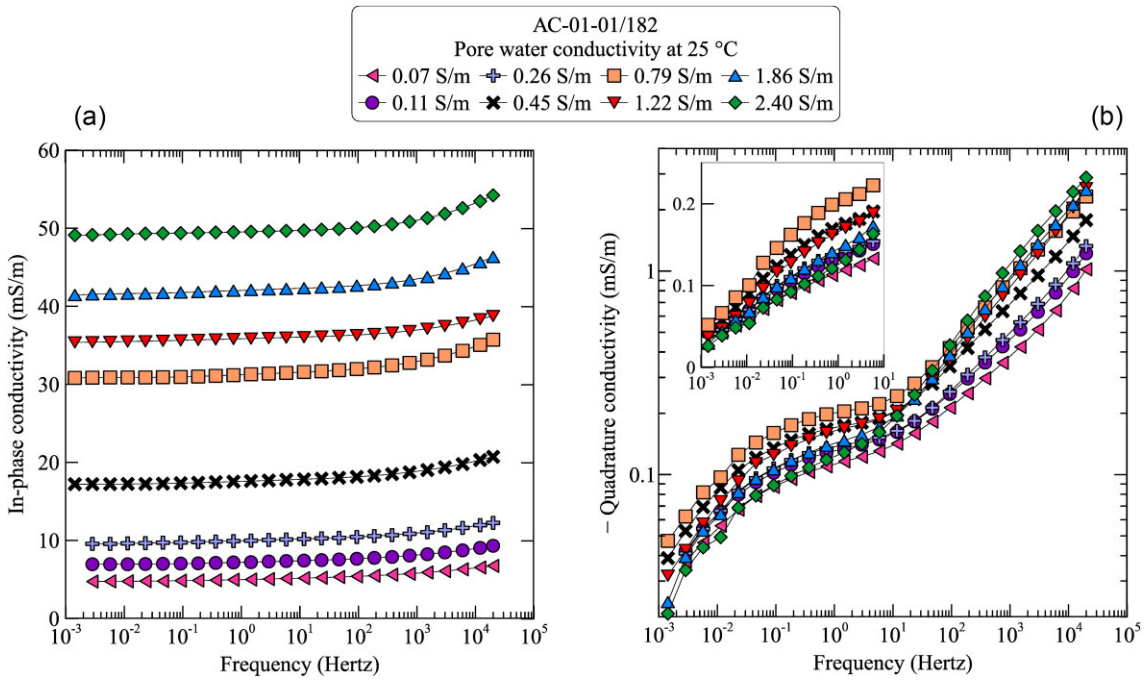

Figure 4. (a) Real and (b) imaginary conductivity spectra of the porphyritic kimberlite sample AC-01–01/182 measured at 11 water conductivity values. The inset in (b) shows the close view to the low-frequency range data.

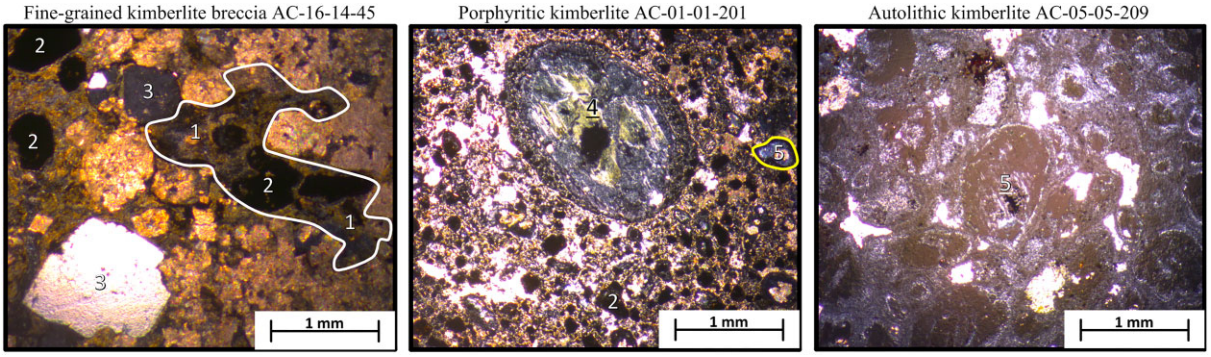

Figure 5. Thin sections of three selected samples (cross-polarized light). The fine-grained breccia, left-hand panel), porphyritic kimberlite (middle panel) and autolithic kimberlite breccia (right-hand panel). 1—groundmass made of smectite and calcite with ore minerals, 2—perovskite, 3—quartz, 4—serpentinized autolith and 5—pseudo-morph of serpentine after the olivine grains. In the middle panel, numerous black particles are ore minerals.

where a (in S × 100 g·meq^{-1}), and the dimensionless number R are proportionality coefficients that depends on the apparent mobilities entering normalized chargeability and surface conductivity relationships (see Revil *et al*. 2013a, b and references therein). Additionally, for the case of the constant phase angle (CPA model), we have additional expressions given by (Weller *et al.* 2013; Revil *et al*. 2017a, b, c)

$$M_n = -\alpha\sigma''. \tag{15}$$

$$\sigma'' = -\frac{R}{\alpha}\sigma_s = -l\sigma'_s, \tag{16}$$

where dimensionless α is the proportionality coefficient. Even eqs (15) and (16) have been derived for the CPA model, they are approximately valid for rather flat spectra. Typically, different authors used σ'' values measured in the frequency range from approximately 1 to 400 Hz.

We measured the amplitude and phase of the impedance using the SIP FUCHS III instrument (radic-research.de) in the frequency range from 1.43 mHz to 20 kHz. Fig. 3(a) shows our measurement cell. We carried out all the measurements in triplicate. Figs 3(b)–(e) show the absolute value and the phase for all the samples obtained at the highest water electrical conductivity value. We demonstrate a very good agreement between the three independent measurements. Such spectra can be modelled with a double Cole–Cole model in complex conductivity (Revil *et al.* 2023a, b) with a low-frequency Cole–Cole contribution associated with the induced polarization component and a high-frequency Cole–Cole model associated with the Maxwell–Wagner polarization or possibly with electromagnetic coupling effects in the measurement device.

Fig. 4 shows an example of the complex electrical conductivity spectra for the sample AC-01–01/182 measured at different water conductivity values. Obviously, with increased water conductivity, the in-phase (real) conductivity of the sample also increases. It

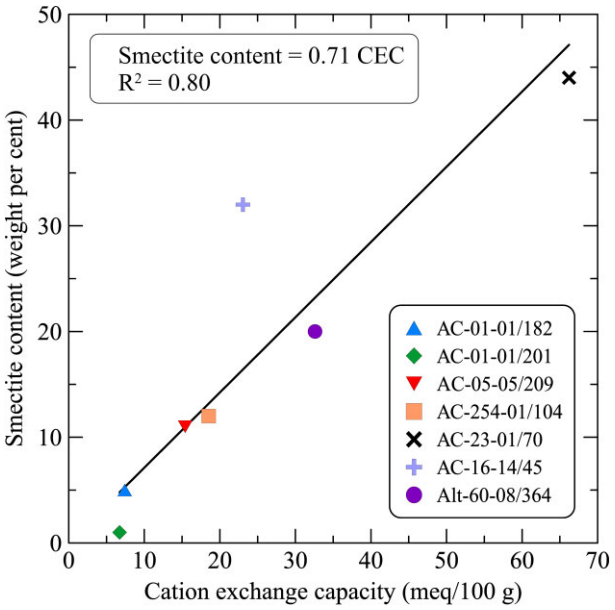

Figure 6. Smectite weight content versus CEC. Symbols identify the samples: AC-01–01/182 and AC-01–01/201 are the porphyritic kimberlites; AC-05–05/209, AC-254–01/104 and AC-23–01/70 are the autolithic kimberlite; AC-16–14/45 is the fine-grained breccia and Alt-60–08/364 is the tuff sandstone with kimberlite material.

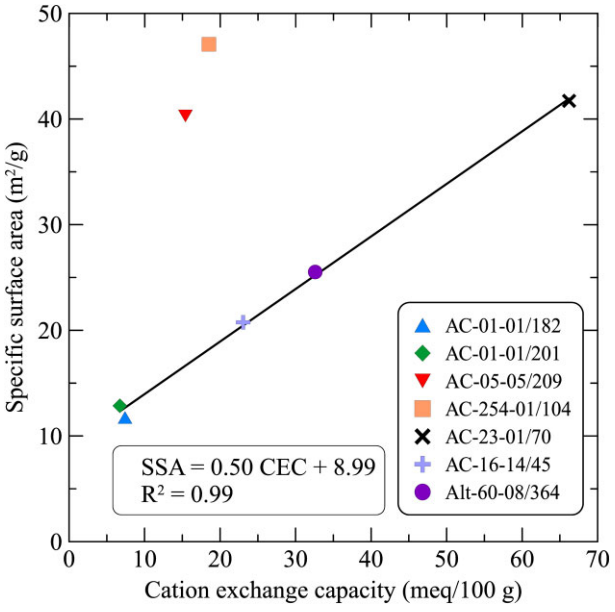

Figure 7. SSA versus CEC. The two outliners were not considered in the data approximation by the linear trend. Symbols identify the samples: AC-01–01/182 and AC-01–01/201 are the porphyritic kimberlites; AC-05–05/209, AC-254–01/104 and AC-23–01/70 are the autolithic kimberlite; AC-16–14/45 is the fine-grained breccia and Alt-60–08/364 is the tuff sandstone with kimberlite material.

also increases with frequency, which reflects the polarization effect. The quadrature conductivity spectra obtained at different frequencies show similar shapes. Regarding the local σ'' values, in low-frequency range (e.g. at about 1 Hz) they first increase with the water conductivity, then reach a maximum at about 0.5 S m^{-1}, and, finally start to decrease with further increase of the water conductivity.

3 RESULTS

3.1. Mineralogical composition

Kimberlites are known as very heterogeneous rocks consisting of groundmass, matrix and inclusions (as mentioned above in the introduction). Kimberlite breccia also contains fragments of rocks surrounding kimberlite bodies (e.g. Mitchell *et al.* 2019; Smit & Shirey 2019). Fig. 5 shows thin sections of three selected core samples: the fine-grained breccia, the porphyric kimberlite and the autolithic kimberlite. The fine-grained breccia is mostly composed by the clay and clay-calcite groundmass filled with numerous ore mineral inclusions. Perovskite and quartz particles are detected in minor quantity (Fig. 5, left-hand panel). The porphyritic kimberlite presents serpentine groundmass contained inclusions of ore minerals (magnetite, haematite and perovskite). Grains of calcite, and numerous pseudo-morphs of serpentine after olivine grains are also detected (Fig. 5, middle panel). The autolithic kimberlite also shows numerous pseudo-morphs of serpentine after olivine grains suspended in the groundmass. The groundmass is built of serpentine with minor content of small dark inclusions of iron minerals (Fig. 5, right-hand panel).

Table 1 provides the mineralogical composition obtained with XRD and TGA methods. These data are in qualitative agreement with the optical microscopy images. Therefore, according to both the optical microscopy and the XRD data, the groundmass presents serpentine, calcite and smectite in various amounts. Small inclusions of iron minerals (haematite or magnetite) are also detected. Greater inclusions represent serpentine pseudo-morphs after the olivine grains. They are frequently surrounded by a thin (∼0.02 mm in average) magnetite (or haematite and perovskite) shells. However, our mineralogical data did not allow distinguishing between the magnetite and other iron minerals; therefore, we consider clarifying this aspect later on the basis of comparison of mineralogical data and MS values. The mineralogical composition suggests two possible causes for the high complex electrical conductivity: the magnetite or the smectite.

Revil *et al.* (2015a) developed an expression for the chargeability of a mixture of a clay-rich matrix in which is embedded metallic particles. The chargeability is determined as a function of the chargeability of the clay-rich matrix and the chargeability associated with the volume fraction of metallic particles. A sensitivity analysis demonstrates that above a critical value (which depends on the CEC of the clay-rich matrix), the amount of metallic particles does not show any influence on the effective chargeability of the mixture. For a smectite-rich matrix, the chargeability of the matrix is close to 0.10 and this critical value is close to 4 per cent in volume fraction. In the present case, the volume content of magnetite is smaller than 5 per cent (vol. fraction) and therefore its influence is expected to be negligible, which will be demonstrated below.

3.2. Cation exchange capacity, specific surface area and magnetic susceptibility

Table 2 shows values of the physical–chemical parameters of the studied core samples. Fig. 6 shows relationship between the smectite content and CEC. Strong linear relationships between these parameters confirms that smectite presents the main cation exchangeable mineral in the mineral assemblage.

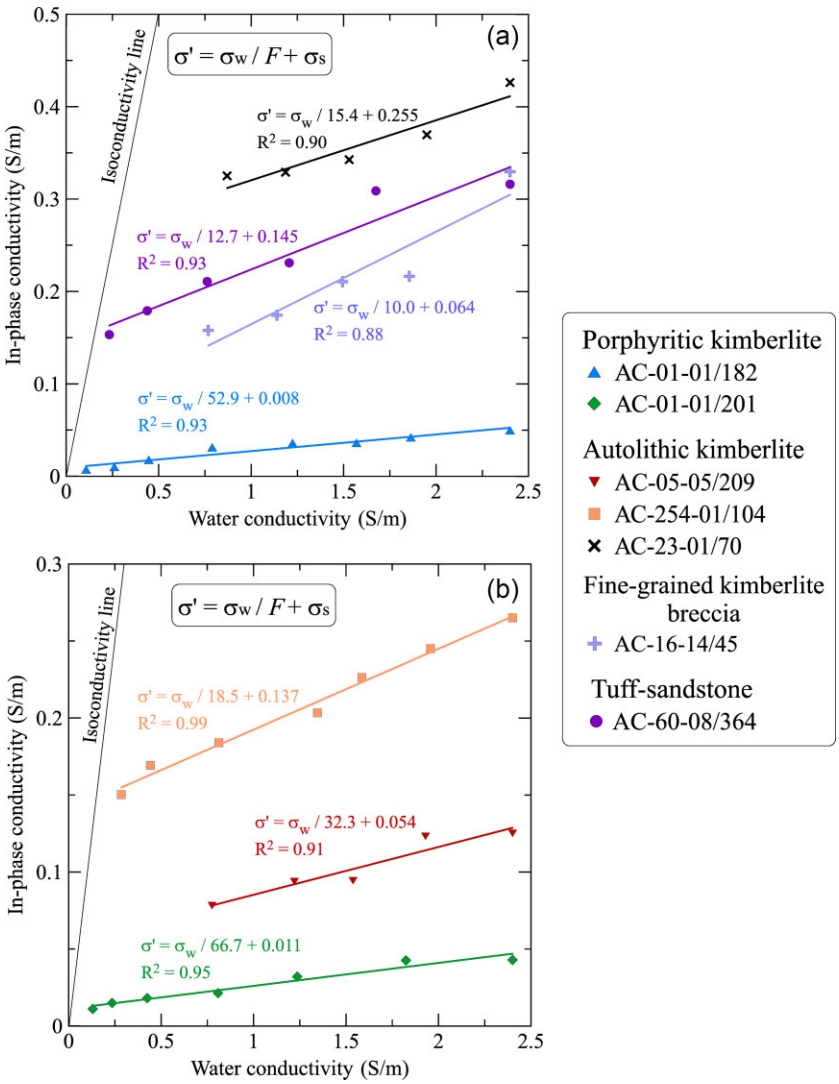

Figure 8. Real part of the complex conductivity at 1.46 Hz versus water conductivity. Symbols identify the samples: AC-01–01/182 and AC-01–01/201 are the porphyritic kimberlites; AC-05–05/209, AC-254–01/104 and AC-23–01/70 are the autolithic kimberlite; AC-16–14/45 is the fine-grained breccia; and Alt-60–08/364 is the tuff sandstone with kimberlite material.

Fig. 7 shows relationship between SSA and CEC. A very good correlation between the parameters is observed except for two samples. However, recalling a high degree of heterogeneity of kimberlite, and the fact that SSA and CEC analyses have been made with separate small subsamples, the presence of such outliers may be explained. Somehow, it is a good surprise that the rest of the core samples exhibits such high degree of correlation between SSA and CEC. Comparing Figs 6 and 7, we recognize that SSA is mostly determined by the smectite content, and that SSA, CEC and the smectite content are all interrelated by linear trends.

The MS values of the core samples are provides in Table 2. The samples show very different values of the MS ranging from 3.1×10^{-4} to 12×10^{-2} SI. MS correlates with the content of magnetite (or haematite) obtained with XRD (not shown for brevity). Therefore, we consider that iron minerals in our samples are dominated by magnetite. However, the MS does not correlate with any other parameters shown in Table 2 (not shown for brevity) indicating again the minor role of magnetite in the induced polarization properties of the core samples.

3.4. Spectral induced polarization

Fig. 8 shows the real part of the conductivity (at 1.46 Hz) versus pore water conductivity. Fig. 8 shows that actually different samples were measured in different water conductivity range. Thus for two porphyric kimberlites (AC-01–01/182 and AC-01–01/204), we obtained the data in the whole planned water conductivity range, whereas for the rest of the core samples, we had to achieve the measurements at conductivity values higher than that we initially planned (between 0.23 and 0.78 S m^{-1}). We had to finish measurements because the samples started to disintegrate likely because of an increased swelling pressure. Nevertheless, the data show reasonable values of the determination coefficients. According to eq. (7), we approximated the data by linear trends to determine the formation factor and the surface conductivity values (reported in Table 2).

Fig. 9(a) shows the relationship between the surface conductivity and the CEC. The data present a good correlation. Fig. 8(b) shows similar relationship with the reduced CEC (normalized to the electrical tortuosity, $F\phi$, according to the model by Revil 2013a). The

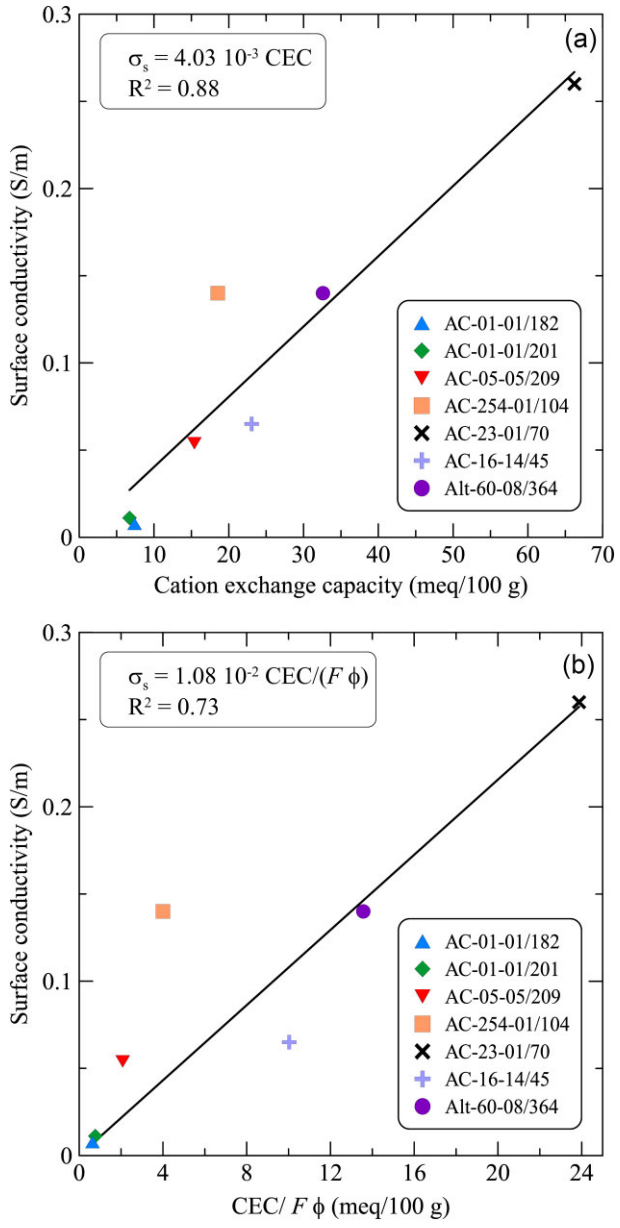

Figure 9. (a) Surface conductivity versus CEC, and (b) CEC normalized to the electrical tortuosity. Symbols identify the samples: AC-01–01/182 and AC-01–01/201 are the porphyritic kimberlites; AC-05–05/209, AC-254–01/104 and AC-23–01/70 are the autolithic kimberlite; AC-16–14/45 is the fine-grained breccia and Alt-60–08/364 is the tuff sandstone with kimberlite material.

data also show a significant correlation; however, the determination coefficient is lower compared to that obtained in Fig. 9(a).

Fig. 10 shows relationship between the normalized chargeability and the imaginary conductivity at 1.46 Hz for all water salinity values. The data present strong correlation according to the proportionality equation (eq. 13). Fig. 11 shows relationships between the normalized chargeability, the quadrature conductivity and the surface conductivity. Both data sets show significant correlations. This means that the global and local measures of the polarization are interrelated with the surface conductivity as discussed in the previous papers of this series.

Fig. 12 shows spectra of the imaginary part of the complex conductivity. The porphyritic kimberlite spectra both present

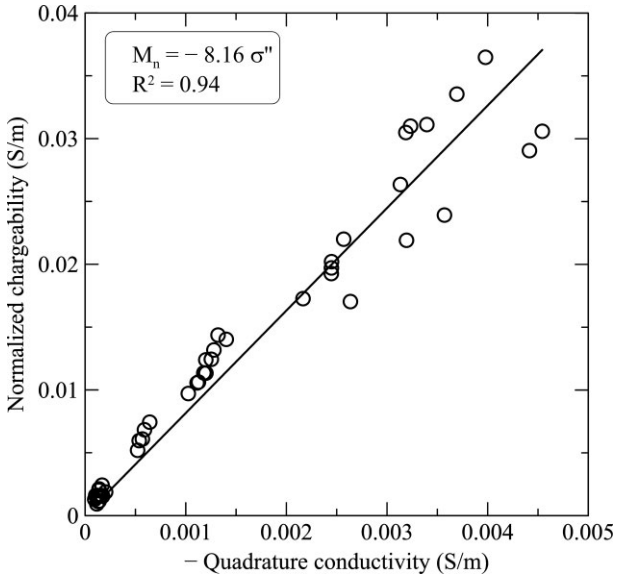

Figure 10. Normalized chargeability versus quadrature conductivity at 1.46 Hz for all samples, and all water electrical conductivity values. The scattering is due to the variations of the quadrature conductivity over frequency.

monotonous increase of the conductivity with frequency (Fig. 12a). One sample of the autolithic kimberlite shows a pronounced peak at the frequency of about 0.1 Hz. Another sample shows a flat and small maximum at about 0.01 Hz. The third sample shows a monotonous increase of the conductivity with frequency (Fig. 12b). The tuff sandstone with kimberlite material and the fine-grained breccia both show maxima at the frequency of about 1 and 23 Hz, respectively (Fig. 12c).

4 DISCUSSION

The values of the imaginary conductivity of the samples (which characterizes the magnitude of the polarization effect) are in the range from 1.05×10^{-4} to 3.98×10^{-3} S m^{-1}. The causes of the elevated magnitude of polarization may be (i) presence of semiconducting magnetite, or (ii) high polarization of the clay-rich groundmass. Therefore, first, we must determine the nature of the IP mechanism: metallic particles versus ion-conducting groundmass.

Even the XRD analysis does not allow us to distinguish between the magnetite and haematite, large values of the MS amounting to 1.21×10^{-2} SI clearly show the presence of magnetite. The largest values of the MS are detected for the porphyritic kimberlite samples (AC-01–01/182 and AC-01–01/201), which, however, show the lowest values of the imaginary conductivity. For the whole data set, the MS does not correlate with the electrical parameters. In addition, considering magnetite as the cause of polarization we would expect a strong relationship between a position of the peak frequency of imaginary conductivity (for the samples containing such peaks) and the pore water conductivity (e.g. Gurin *et al.* 2015). However, for the samples containing peaks in the imaginary conductivity spectra, the peak location is virtually constant (not shown for brevity). The magnetite presents fine particles, which probably present maxima of the quadrature conductivity spectra in the high-frequency range outside the operation window of our SIP measurements. Revil and co-workers (Revil *et al.* 2017a) also found that about 5 per cent of magnetite does not increase polarization of volcanic rocks (see also Revil *et al.* 2015a).

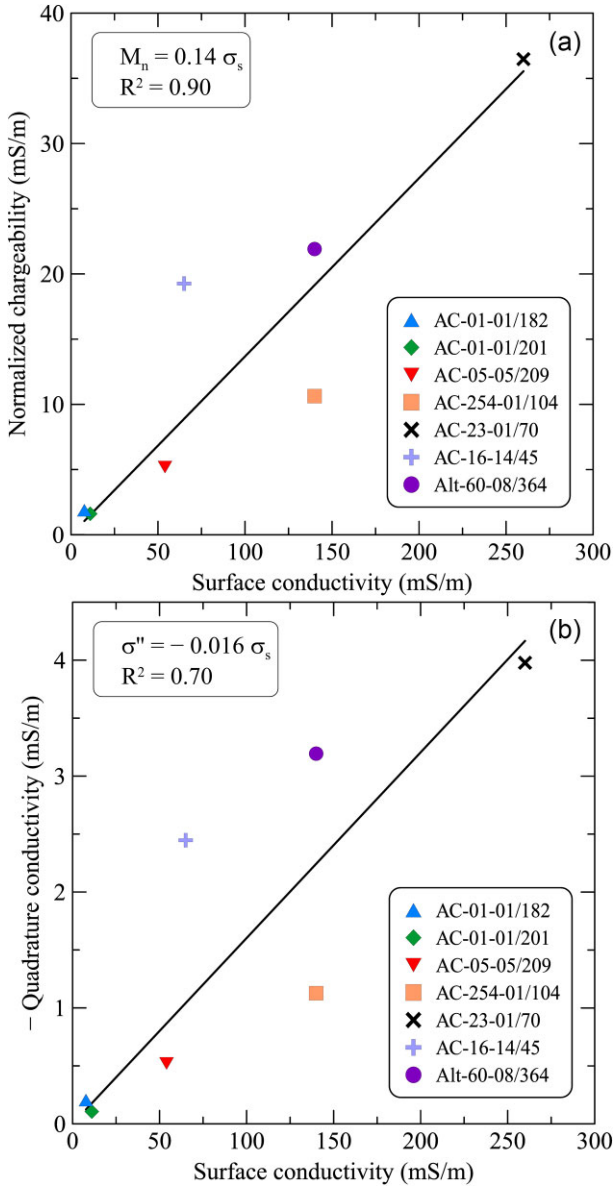

Figure 11. (a) Normalized chargeability and (b) quadrature conductivity at 1.46 Hz versus real part of the surface conductivity. The water conductivity is approximately 0.8 S m^{-1}. Lower determination coefficient in panel (b) comparing to panel (a) is due to the variations of the quadrature conductivity over frequency. Symbols identify the samples: AC-01–01/182 and AC-01–01/201 are the porphyritic kimberlites; AC-05–05/209, AC-254–01/104 and AC-23–01/70 are the autolithic kimberlite; AC-16–14/45 is the fine-grained breccia and Alt-60–08/364 is the tuff sandstone with kimberlite material.

According to the aforementioned argumentation, the IP effect of the studied kimberlite samples is associated with the polarization of the Stern layer (e.g. Leroy *et al.* 2008) or the membrane polarization (e.g. Titov *et al.* 2002). Close linear or proportionality relationships between the surface conductivity, quadrature conductivity, normalized chargeability, SSA, CEC and the smectite content (Figs 6, 7, 9–11) also confirm our hypothesis of the Stern layer model.

The smectite content is proportional to CEC (Fig. 6). The slope of this relationship is consistent with previously published data for soils (Revil *et al.* 2017b) and for volcanic rocks (Levy *et al.* 2018; Revil et al 2018, 2019). The values of SSA and CEC follow the linear trend. Both relationships indicate the degree of alteration of the kimberlite: the larger the alteration degree, the larger the smectite content, the CEC and SSA values. The real part of the surface conductivity is proportional to the ratio of CEC and electrical tortuosity (Fig. 9b). These data are in accordance with the model in Revil (2013a, his eq. 80; see also Revil 2013b).

In addition, our data show that three electrical parameters, the surface conductivity, the normalized chargeability and the quadrature conductivity are all interrelated and proportional (Figs 10 and 11). The determination coefficient is slightly smaller for the relationship '$\sigma'' - \sigma_s$' comparing to the rest of relationships; however this can be explained because the phase varies over frequency (while a constant phase was assumed in the theory, Revil 2013a).

The proportionality between the electrical parameters is in accordance with theoretical predictions (Revil 2013a, b; Revil *et al.* 2015b), and with empirical data (Börner *et al.* 1996; Weller *et al.* 2013). The coefficients obtained for our collection are in satisfactory agreement with previously published data especially for volcanic rocks. Only exception is the data set of Lévy *et al.* (2019), who found sufficiently smaller values of the *l*-parameter for smectite-rich volcanic rocks (>10 vol. per cent). We did not observe such behaviour. Lévy *et al.* (2019) interpreted the decrease of the *l*-coefficient by the decrease of the polarization with respect to the surface conduction because of interfoliar conduction in smectite. A model of such conduction is rather the capillary model than the granular one. For the capillary model, the membrane polarization mechanism probably dominates, whereas for the granular model the Stern layer polarization is the main governing mechanism, even the membrane polarization is also present (Emelianov *et al.* 2023, under review). Accordingly, regarding the relationships '$\sigma'' - \sigma_s$', '$M_n - \sigma''$' and '$M_n - \sigma_s$', we believe that the Stern layer polarization does govern SIP response of kimberlite.

Fig. 13 shows relationship between the normalized chargeability and the surface conductivity for kimberlite samples along with the relationship for soils and basalts with different degree of alteration. Fig. 13 clearly show that electrical properties of the kimberlites fall in the same trend as other rocks and soils. Their electrical behaviour is determined by the surface conductivity effect, which is responsible for both conduction and polarization.

From the practical point of view, the quadrature conductivity or the normalized chargeability can be used to obtain the smectite content (Fig. 14). In Fig. 14, we present the smectite content versus normalized chargeability (Fig. 14a) and versus quadrature conductivity measured at 94 Hz (Fig. 14b). The normalized chargeability shows a good linear correlation with the smectite content. However, the quadrature conductivity at 94 Hz shows nonlinear behaviour, but, surprisingly, no data scattering. We believe that the high-frequency (hundreds of hertz) quadrature conductivity could be more appropriate to assess the clay content, but for our collection, a risk of the data 'contamination' by high-frequency response of small magnetite particles still exists. That is why we have based our analysis mostly on the quadrature conductivity measured at 1.46 Hz. Anyway, we interpret this nonlinear behaviour as follows. At low smectite content (up to 11 per cent), the polarization is determined by serpentine, quartz particles and, probably to some extend by magnetite. Starting from about 18 per cent, the quadrature conductivity nonlinearly increases with increase of the smectite content. With further increase of the smectite content, this relationship can reach an asymptote, or present a maximum, but our data does not allow clarifying this behaviour.

The assessment of the smectite content can help not only to detect kimberlites, but also to distinguish between the kimberlite facies

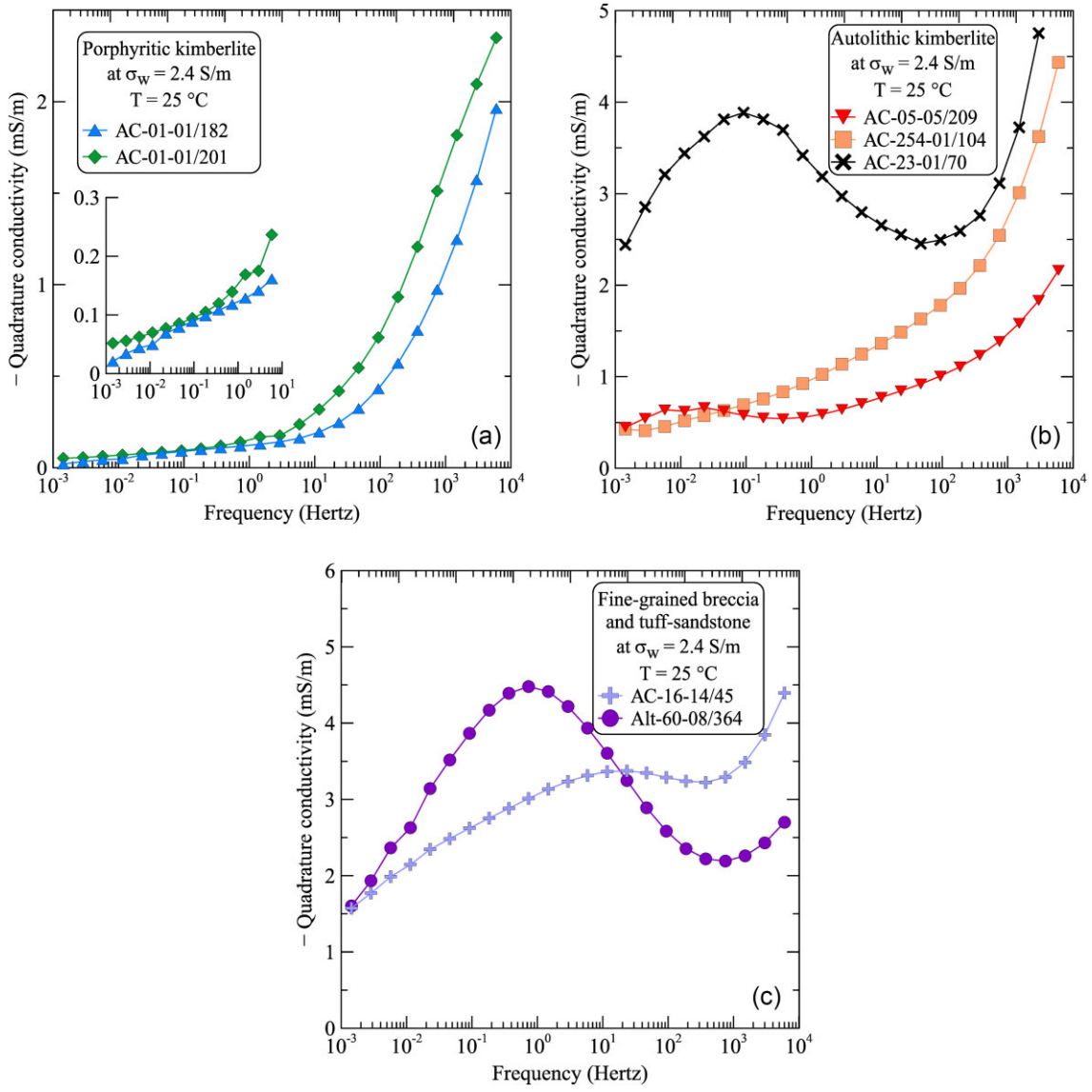

Figure 12. Spectra of the quadrature conductivity at the water conductivity of 2.4 S m^{-1}. The inset in (a) shows magnification of the spectra at low-frequency range. Symbols identify the samples: AC-01–01/182 and AC-01–01/201 are the porphyritic kimberlites; AC-05–05/209, AC-254–01/104 and AC-23–01/70 are the autolithic kimberlite; AC-16–14/45 is the fine-grained breccia and Alt-60–08/364 is the tuff sandstone with kimberlite material.

(e.g. rich in smectite versus rich in serpentine, olivine or calcite). This distinguishing is important, in particular, because different kimberlite facies may have different diamond grade. This opens the door for using SIP method in kimberlite exploration with surface or borehole measurements. Cross-correlation plots combined with clustering techniques could help in defining high diamond grade kimberlites, but this is not of the task of the present paper to go in this direction.

We now discuss what elements of the pore space are responsible for the polarization of the kimberlites? Among the three autolithic kimberlite samples, two samples show peaks at about 0.09 and 0.01 Hz, and one sample shows monotonous spectrum similar in shape to those of the porphyritic kimberlite, but with larger magnitude. The tuff-sandstone and the fine-grained breccia samples also show clear peaks at 0.73 and 23 Hz, respectively. Assuming polarization of the Stern layer around a spherical grain (e.g. Schwarz 1962; Revil *et al.* 2015b), the grain radius is related to the relaxation time ($\tau = 1/2\pi f_{\text{peak}}$) as

$$r = \sqrt{2 D_s \tau}, \tag{17}$$

where D_s is the cation diffusivity in the Stern layer. Let us now assess the grain radius for the largest and smallest relaxation time values detected in the spectra. We obtain the largest relaxation time, $\tau = 14.0$ s, for the autolytic kimberlite (AC-05–05/209). Regarding the mineral composition, its groundmass is dominated by serpentine (76 wt. per cent, see Table 1). Having no data about the cation diffusivity in the Stern layer of serpentine, let us assume that it has the same value as for the quartz surface, namely, $D_s = 1.3 \times 10^{-9}$ m^2 s^{-1} (Na^+ at 25 °C). Applying eq. (17), we obtain $r = 0.2$ mm, in remarkably agreement with the radii of the pseudo-morphs of serpentine after the olivine grains detected by optical microscopy (Fig. 5, right-hand panel).

The smallest relaxation time, $\tau = 6.90 \cdot 10^{-3}$ s, was detected for the fine-grained breccia (AC-16–14/45). Here the major

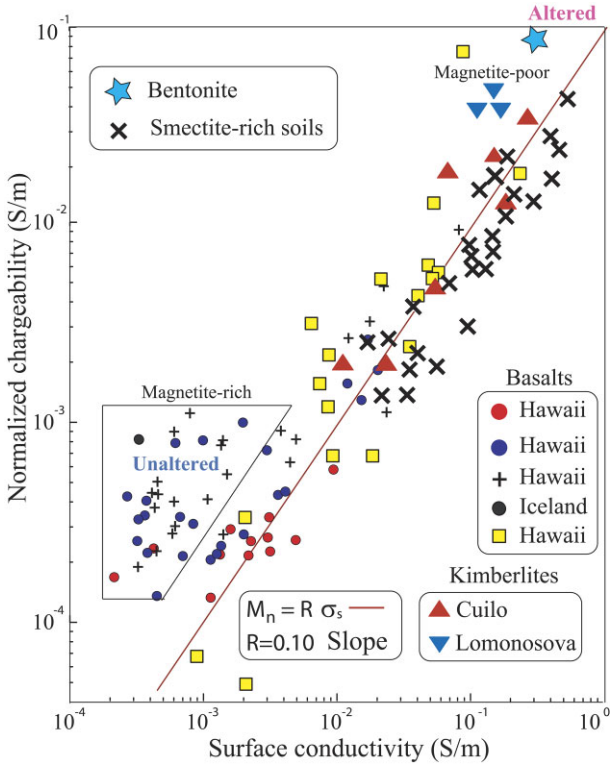

Figure 13. Quadrature conductivity versus surface conductivity for sedimentary rocks, basalts, soils and kimberlites (modified from Revil *et al.* 2021). Symbols: red-filled circle—surface samples at Kilauea (Hawaii); blue-filled circle—well K-W at Kilauea (Hawaii); plus—well PTA-2 at Kilauea (Hawaii); black-filled circle—at Krafla (Hawaii) and yellow-filled circle—well SOH-2 at Hawaii.

components are smectite (32 wt. per cent), quartz (34 wt. per cent) and calcite (15 wt. per cent). To explain the polarization of this sample we have to choose between these three candidates. Because calcite at pH about 7 shows approximately one order of magnitude smaller polarization than that of phyllosilicates (Panwar *et al.* 2021), we can safely neglect its impact to the sample polarization. Two other candidates are smectite and quartz. Assuming first that quartz is responsible for the peak in the spectra, and using ones again the value of the surface diffusivity, $D_s = 1.3 \times 10^{-9}$ m^{2}s^{-1}, we obtain $r = 4.2 \times 10^{-3}$ mm. This value is inconsistent with optical microscopy image showing the quartz grains with radii of about 0.7 mm or slightly less (Fig. 5, left-hand panel). Therefore, we must attribute polarization to the smectite groundmass seen in the image. Applying $D_s = 3.8 \times 10^{-12}$ m^2 s^{-1} for smectite surfaces, we obtain $r = 3.2 \times 10^{-4}$ mm. This submicrometre value is practically out of resolution limit of the optical microscopy. It could be resolved based on the computing nanotomography or scanning electron microscopy. However, we consider this task to be the subject of a separate study.

5 CONCLUSIONS

We have studied the complex conductivity spectra and the MS of 7 core samples of kimberlites. To our knowledge, this is the first study regarding the induced polarization properties of kimberlites. From our results, the following conclusions have been reached.

(1) Even the kimberlite contains significant amount of magnetite, its induced polarization is caused by the smectite-rich groundmass.

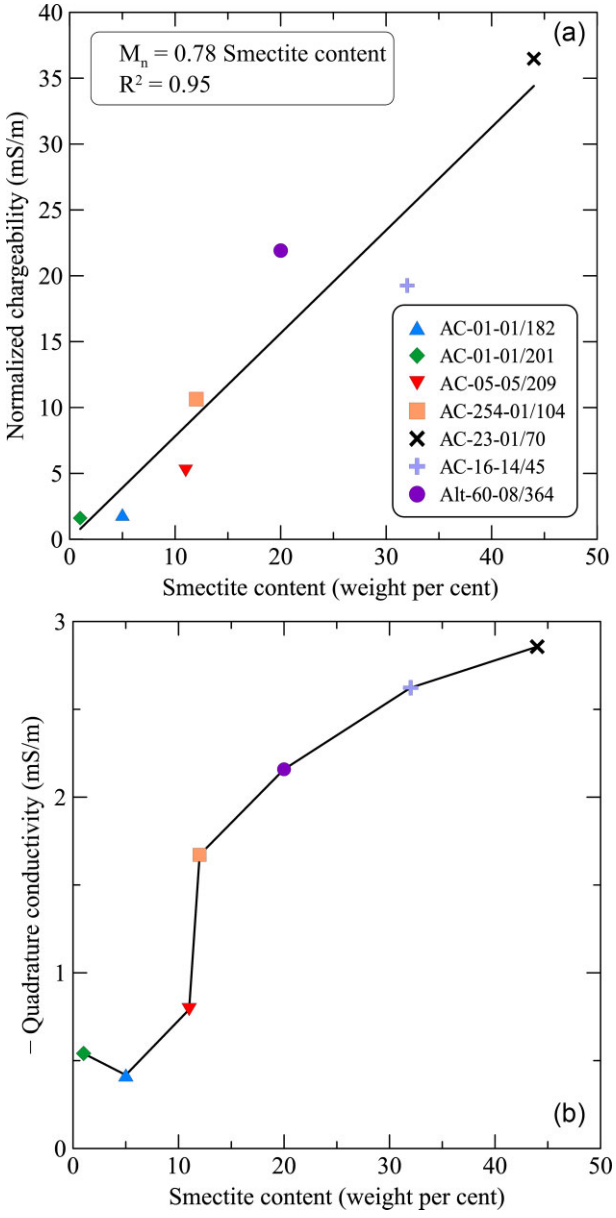

Figure 14. Normalized chargeability. (a) Normalized chargeability versus quadrature conductivity at 94 Hz (plain line: best linear fit). (b) Normalized chargeability versus smectite weight content (the line is just a guide for the eyes). Symbols identify the samples: AC-01–01/182 and AC-01–01/201 are the porphyritic kimberlites; AC-05–05/209, AC-254–01/104 and AC-23–01/70 are the autolithic kimberlite; AC-16–14/45 is the fine-grained breccia and Alt-60–08/364 is the tuff sandstone with kimberlite material.

(2) At least for low pore water salinity, the electrical conductivity of kimberlite is dominated by its surface conductivity. The electrical properties of the kimberlites are similar to that of altered volcanic rocks, clayey sandstones and soils. With increased degree of alteration, both the basalts and kimberlites show an increase of smectite content, CEC, SSA, surface and quadrature conductivity as well as the normalized chargeability.

(3) The aforementioned parameters are all interrelated. The proportionality coefficients in the relationships '$M_n - CEC/F\phi$', '$M_n - \sigma''$', '$\sigma'' - \sigma'_s$' and '$M_n - \sigma'_s$' for the kimberlites, the previously studied volcanic rocks and clayey sandstones are in remarkable agreement, which confirms that the kimberlite polarization is

due to the Stern layer polarization according to the dynamic Stern layer model.

(4) Our petrophysical investigations explain the cause of electrical anomalies frequently observed in the realm of the geoelectrical exploration of kimberlites across the world. Furthermore, we argue for the use of the induced polarization method in kimberlites exploration, which has a potential to distinguish between the different facies of kimberlites.

Our future investigations will include the effect of ice for applications to Arctic areas. In this case, the induced polarization properties of icy materials is influenced by the presence of ice (Revil *et al.* 2019) and ice itself (a dirty proton-based semi-conductor) would polarize at high frequencies (around 10 kHz, see Duvillard *et al.* 2018). This would be important to interpret airborne time-domain electromagnetic data in such environments (Kang *et al.* 2017).

ACKNOWLEDGMENTS

This work was supported by Russian Science Foundation through the grant no. 20–47–04402 'Development of the induced polarization theory with application to exploration of strategic raw materials'. We thank the editor and the two referees for their very constructive reviews of our manuscript. We thank our colleagues from the 'Center for Innovative Technologies of Composite Nanomaterials', and the 'Center of X-ray diffraction studies' at the Research park of St. Petersburg State University for carrying out physical–chemical measurements. We thank the 'Geomodel Center' at the same Research Park for permission to use SIP FUCHS III instrument. We thank JSC 'Alrosa' for providing us with the core samples of kimberlite.

DATA AVAILABILITY

The data presented in this paper are available upon request to the corresponding author.

CONFLICT OF INTEREST

There is no conflict of interest.

REFERENCES

Afanasyev, A.A., Melnik, O., Porritt, L., Schumacher, J.C. & Sparks, R.S.J., 2014. Hydrothermal alteration of kimberlite by convective flows of external water, *Contrib. Mineral. Petrol.,* **168(1)**(1), 10.1007/s00410-014-1038-y.

Archie, G.E., 1942. The electrical resistivity log as an aid in determining some reservoir characteristics, *Trans. Am. Inst. Min. Metall. Pet. Eng.,* **146,** 54–62. 10.2118/942054-G.

Börner, F.D., Schopper, J.R. & Weller, A., 1996. Evaluation of transport and storage properties in the soil and groundwater zone from induced polarization measurements, *Geophysical Prospecting,* **44,** 583–601. 10.1111/j.1365-2478.1996.tb00167.x.

Brunauer, S., Emmett, P. & Teller, E., 1938. Adsorption of gases in multimolecular layers, *J. Am. Chem. Soc.,* **60,** 309–319. 10.1021/ja01269a023.

Coats, A.W. & Redfern, J.P., 1963. Thermogravimetric analysis: a review, *Analyst,* **88,** 906–924. 10.1039/an9638800906.

Cole, K.S. & Cole, R.H., 1941. Dispersion and absorption in dielectrics — I. Alternating current characteristics, *J. Chem. Phys.,* **9,** 341–351. 10.1063/1.1750906.

Coopersmith, H., Pell, J. & Smith, B., 2006. The importance of Kimberlite geology in diamond deposit evaluation: a case study from the DO27/DO18 Kimberlite, NWT, Canada, in *in Extended Abstracts: 8th International Kimberlite Conference, Saskatoon, Canada*.

Cruz, S.E.R., 2012. *Kimberlites Associated with the Lucapa Structure, Angola,* PhD thesis, Barcelona University.

Debye, P., 1929. *Polar Molecules,* The Chemical Catalogue Company, New York.

Duvillard, P.A., Revil, A., Soueid Ahmed, A., Qi, Y., Coperey, A. & Ravanel, L., 2018. Three-dimensional electrical conductivity and induced polarization tomography of a rock glacier, *J. geophys. Res.,* **123,** 9528–9554. 10.1029/2018JB015965.

Eley, R., Grütter, H., Louw, A., Tunguno, C. & Twidale, J., 2008. Exploration geology of the Luxinga kimberlite cluster (Angola) with evidence supporting the presence of kimberlite lava, in *Extended Abstracts: 9th International Kimberlite Conference,* doi:10.29173/ikc3410.

Emelianov, V., Zhang, Z., Weller, A., Halisch, M. & Titov, K., 2023. Surface conductivity of clays, *Geophys. J. Int.,* submitted.

Emelyanov, V.I., Titov, K.V. & Revil, A., 2020. Surface conductivity and induced polarization of Kimberlite, in *Conference Proceedings, Engineering and Mining Geophysics, Sep 2020,* pp. 1–6. In review.

Field, M. & Scott Smith, B.H., 1999. Contrasting geology and near-surface emplacement of kimberlites in southern Africa and Canada, in *Proceedings of the 7th International Kimberlite Conference,* Vol. **1,** pp. 214–237.

Gurin, G., Titov, K., Ilyin, Y.. & Tarasov, A., 2015. Induced polarization of disseminated electronically conductive minerals: a semi-empirical model, *Geophys. J. Int.,* **200,** 1555–1565. 10.1093/gji/ggu490.

Hawthorne, J.B., 1975. Model of a kimberlite pipe, *Phys. Chem. Earth,* **9,** 1–15. 10.1016/0079-1946(75)90002-6.

Ji, S. *et al.*, 2018. Conversion of serpentine to smectite under hydrothermal condition: implication for solid-state transformation, *Am. Mineral.,* **103,** 241–251. 10.2138/am-2018-6183CCBYNCND.

Jougnot, D., Ghorbani, A., Revil, A., Leroy, P. & Cosenza, P., 2010. Spectral induced polarization of partially saturated clay-rocks: a mechanistic approach, *Geophys. J. Int.,* **180,** 210–224. 10.1111/j.1365-246X.2009.04426.x.

Kan, R. & Sen, P.N., 1987. Electrolytic conduction in periodic arrays of insulators with charges, *J. Chem. Phys.,* **86,** 5748–5756. 10.1063/1.452502.

Kang, S., Dominique, F. & Oldenburg, D., 2017. Inversion of airborne geophysics over the DO-27/18 kimberlites, part III: induced polarization, *Interpretation,* **5,** 1–48. 10.1190/INT-2017-0815-ERRATUM.1.

Katsube, T.J. & Scromeda, N., 1994. Physical properties of Canadian kimberlites, Somerset Island, Northwest Territories and Saskatchewan, in *Current Research 1994-B, Geological Survey of Canada,* pp. 35–42.

Kjarsgaard, B.A., 2003. Volcanology of Kimberlite, in *Diamonds Short Course Notes,* Tosdal, R.(ed.), Cordilleran Round-Up, Vancouver, B.C., January 29–30, 20pp.

Kjarsgaard, B.A., 2007. Kimberlite Pipe models: significance for exploration, in *Proceedings of Exploration 07: Fifth Decennial International Conference on Mineral Exploration,* pp. Milkereit, B.(ed.), 667–677.

Kononova, V.A., Golubeva, Y..Y.., Bogatikov, O.A. & Kargin, A.V., 2007. Diamond resource potential of kimberlites from the Zimny Bereg Field, Arkhangel'sk Oblast, *Geol. Ore Deposits,* **49,** 421–441. 10.1134/S1075701507060013.

Kralchevsky, P.A., Danov, D.D. & Denkov, N.D., 2008. Chemical physics of colloid systems and interfaces, in *Handbook of Surface and Colloid Chemistry,* 3rd edn, Birdi, K.S.(ed.). Taylor & Francis Group, LLC, Boca Raton.

Leroy, P., Revil, A., Kemna, A., Cosenza, P. & Ghorbani, A., 2008. Complex conductivity of water-saturated packs of glass beads, *J. Colloid Interf. Sci.,* **321,** 103–117. 10.1016/j.jcis.2007.12.031.

Lévy, L., Gibert, B., Sigmundsson, F., Flóvenz, G., Herisher, G.P., Briole, P. & Pezard, P.A., 2018. The role of smectites in the electrical conductivity of active hydrothermal systems: electrical properties of core samples from Krafla volcano, Iceland, *Geophys. J. Int.,* **215,** 1558–1582. 10.1093/gji/ggy342.

Lévy, L., Weller, A. & Gibert, B., 2019. Influence of smectite and salinity on the imaginary and surface conductivity of volcanic rocks, *Near Surf. Geophys.,* **17,** 653–673. 10.1002/nsg.12069.

Macnae, J.C., 1979. Kimberlites and exploration geophysics, *Geophysics,* **44**(8), 1395–1416.

Misra, S., Torres-Verdín, C., Revil, A., Rasmus, J. & Homan, D., 2016a. Interfacial polarization of disseminated conductive minerals in absence of redox-active species. Part 1: mechanistic model and validation, *Geophysics,* **81**(2), E139–E157.

Misra, S., Torres-Verdín, C., Revil, A., Rasmus, J. & Homan, D., 2016b. Interfacial polarization of disseminated conductive minerals in absence of redox-active species. Part 2. Effective complex conductivity and dielectric permittivity, *Geophysics,* **81**(2), E159–E176.

Mitchell, R.H., 1986. *Kimberlites: Mineralogy, Geochemistry, and Petrology*. Plenum Press, New York, 442pp.

Mitchell, R.H., 1995. *Kimberlites, Orangeites, and Related Rocks,* Plenum Press, New York, 410pp.

Mitchell, R.H., Giuliani, A. & O'Brien, H., 2019. What is a Kimberlite? Petrology and mineralogy of Hypabyssal Kimberlites, *Elements,* **15**. 381–386. 10.2138/gselements.15.6.381.

Morkel, J. & Vermaak, M.K.G., 2006. The role of swelling clay in kimberlite weathering, *Miner. Process. Extr. Metall.,* **115**(3), 150–154.

Morkel, P.J., Pistorius, P.C. & Vermaak, M.K.G., 2007. Cation exchange behaviour of kimberlite in solutions containing Cu^{2+} and K^{+}, *Miner. Eng.,* **20 (** 12**)**, 1145–1152.

Nordsiek, S. & Weller, A., 2008. A new approach to fitting induced polarization spectra, *Geophysics,* **75,** F235–F245. 10.1190/1.2987412.

Olhoeft, G.R., 1981. Electrical properties of rocks, *Physical Properties of Rocks and Minerals,* pp. 257–297.

Onugba, A., Bello, A. & Ajakaiye, D.E., 1989. Resistivity and seismic refraction survey of the Massari/Kafur "Kimberlite" pipe in Northern Nigeria (and its groundwater reserves), *J. Afr. Earth Sci.,* **9**(2), 235–243.

Panwar, N. *et al.* 2021. Induced polarization of carbonates, *J. geophys. Res.: Solid Earth,* **126,** e2021JB022029, doi: 10.1029/2021JB022029.

Pelton, W.H., Ward, S.H., Hallof, P.G., Sill, W.R. & Nelson, P.H., 1978. Mineral discrimination and removal of inductive coupling with multifrequency IP, *Geophysics,* **43,** 588–609. 10.1190/1.1440839.

Pettit, W., 2009. Geophysical signatures of some recently discovered large (>40 ha) kimberlite pipes on the Alto Cuilo concession in northeastern Angola, *Lithosphere,* **112,** 106–115. 10.1016/j.lithos.2009.05.046.

Power, M., Belcourt, G. & Rockel, E., 2004. Geophysical methods for kimberlite exploration in northern Canada, *Leading Edge,* **11,** 1124–1129. 10.1190/1.1825939.

Reed, L.E. & Witherly, K.E., 2007. 50 Years of Kimberlite geophysics. A review, in *Proceedings of Exploration 07: Fifth Decennial International Conference on Mineral Exploration,* Milkereit, B., ed., pp. 679–689.

Revil, A. *et al.*, 2019. Induced polarization response of porous media with metallic particles – Part 9. Influence of permafrost, *Geophysics,* **84**(5), A43–W32.

Revil, A., 2013a. On charge accumulation in heterogeneous porous rocks under the influence of an external electric field, *Geophysics,* **78,** D271–D291. 10.1190/geo2012-0503.1.

Revil, A., 2013b. Effective conductivity and permittivity of unsaturated porous materials in the frequency range 1 mHz–1 GHz, *Water Resour. Res.,* **49,** 306–327. 10.1029/2012WR012700.

Revil, A., Binley, A., Mejus, L. & Kessouri, P., 2015b. Predicting permeability from the characteristic relaxation time and intrinsic formation factor of complex conductivity spectra, *Water Resour. Res.,* **51,** 6672–6700. 10.1002/2015WR017074.

Revil, A., Florsch, N. & Mao, D., 2015a. Induced polarization response of porous media with metallic particles—Part 1: a theory for disseminated semiconductors, *Geophysics,* **80**(5), D525–D538.

Revil, A., Ghorbani, A., Gailler, L.S., Gresse, M., Panwar, N. & Sharma, R., 2018. Electrical conductivity and induced polarization investigations at Kilauea volcano, Hawai'i, *J. Volc. Geotherm. Res.,* **368,** 31–50. 10.1016/j.jvolgeores.2018.10.014.

Revil, A., Ghorbani, A., Jougnot, D. & Yven, B., 2023a. Induced polarization of clay-rich materials—Part 1: the effect of desiccation, *Geophysics,* **88**(4), MR195–MR210.

Revil, A., Ghorbani, A., Jougnot, D., Yven, B., Grgic, D., Bretaudeau, F. & Deparis, J., 2023b. Induced polarization of clay-rich materials. Part 2. The effect of anisotropy, *Geophysics,* **88**(6), 1–53.

Revil, A. & Glower, P.W.J., 1998. Nature of surface conductivity in natural sands, sandstones and clays, *Geophys. Res. Lett.,* **25,** 691–694. 10.1029/98GL00296.

Revil, A., Le Breton, M., Niu, Q., Wallin, E., Haskins, E. & Thomas, D.M., 2017a. Induced polarization of volcanic rocks –1. Surface versus quadrature conductivity, *Geophys. J. Int.,* **208,** 826–844. 10.1093/gji/ggw444.

Revil, A., Le Breton, M., Niu, Q., Wallin, E., Haskins, E. & Thomas, D.M., 2017b. Induced polarization of volcanic rocks. 2. Influence of pore size and permeability, *Geophys. J. Int.,* **208,** 814–825. 10.1093/gji/ggw382.

Revil, A. *et al.*, 2017c. Complex conductivity of soils, *Water Resour. Res.,* **53,** 7121–7147. 10.1002/2017WR020655.

Revil, A., Qi, Y., Ghorbani, M., Gresse, M. & Thomas, D., 2021. Induced polarization of volcanic rocks. 5. Imaging the temperature field of shield volcanoes, *Geophys. J. Int.,* **225,** 1492–1509. 10.1093/gji/ggab039.

Schwarz, G., 1962. A theory of the low-frequency dielectric dispersion of colloidal particles in electrolyte solution, *J. Phys. Chem.,* **66,** 2636–2642. 10.1021/j100818a067.

Smit, K.V. & Shirey, S.B., 2019. Kimberlites: earth's diamond delivery system, *Gems Gemology,* **55**(2), 270–276. https://www.gia.edu/gems-gemology/spring-2019-how-old-are-diamonds-are-they-forever.

Sparks, R.S.J., Baker, L., Brown, R.J., Field, M., Schumacher, J., Stripp, G. & Walters, A.L. 2006. Dynamics of Kimberlite volcanism, *J. Volc. Geotherm. Res.,* **155,** 18–48. 10.1016/j.jvolgeores.2006.02.010.

Standard, 2022. *Standard Operating Procedure for Cation Exchange Capacity and Exchangeable Bases1 Nammonium Acetate pH 7.0 Method*. Food and Agriculture Organization of the United Nations, Rome.

Titov, K., Komarov, V., Tarasov, V. & Levitski, A., 2002. Theoretical and experimental study of time domain-induced polarization in water-saturated sands, *J. appl. Geophys.,* **50,** 417–433. 10.1016/S0926-9851(02)00168-4.

Titov, K.V., Emelianov, V.I., Abramov, V.Y.. & Revil, A., 2021. Complex electrical conductivity of kimberlite, in *Conference Proceedings, NSG2021 27th European Meeting of Environmental and Engineering Geophysics,* Vol. **2021,** European Association of Geoscientists & Engineers, pp. 1–5.

Waxman, M.H. & Smits, L..J.M., 1968. Electrical conductivities in oil-bearing shaly sands, *SPE J,* **8**(2), 107–122.

Weller, A., Slater, L. & Nordsiek, S., 2013. On the relationship between induced polarization and surface conductivity: implications for petrophysical interpretation of electrical measurements, *Geophysics,* **78,** D315–D325. 10.1190/geo2013-0076.1.

Wong, J., 1979. An electrochemical model of the induced-polarization phenomenon in disseminated sulfide ores, *Geophysics,* **44,** 1245–1265. 10.1190/1.1441005.

Zagainy, A.K., Mikoev, I.I., Ustinov, V.N., Feijo, A. & Antonov, S.A., 2017. Structural-tectonic and geophysical background for the localization of kimberlite in the territory of Angola, *Ores Metals,* **4,** 42–49. (In Russian).

Zhang, K., Chibati, N., Revil, A., Richard, J., Gresse, M., Xue, Y. & Géraud, Y., 2023. Induced polarization of volcanic rocks –6: relationships with other petrophysical properties, *Geophys. J. Int.,* **234,** 2376–2394. 10.1093/gji/ggad103.